Magnetic and geochemical scanning reveals growth history of marine ferromanganese crust on Detroit Seamount, northwest Pacific since the early Miocene

Liang Yi [a,*], Yibing Li [a], Pavel Mikhailik [b], Youqiang Qi [c], Chenglong Deng [d,e]

[a] *State Key Laboratory of Marine Geology, Tongji University, Shanghai, 200092, China*
[b] *Laboratory of Regional Geology and Tectonic, Far East Geological Institute, Far East Branch of Russian Academy of Sciences, Vladivostok, 690022, Russia*
[c] *State Key Laboratory of Ore Deposit Geochemistry, Institute of Geochemistry, Chinese Academy of Sciences, Guiyang, Guizhou, 550081, China*
[d] *State Key Laboratory of Lithospheric Evolution, Institute of Geology and Geophysics, Chinese Academy of Sciences, Beijing, 100029, China*
[e] *University of Chinese Academy of Sciences, Beijing, 100049, China*

ARTICLE INFO

ABSTRACT

The Hawaiian Chain-Emperor Seamounts is known to be one of the most active regions influenced by mantle hotspot. However, previous studies have provided limited information on the growth process and metal enrichment of marine ferromanganese crusts as indicators of post-eruption history. In this study, we conducted a geochronological and major elemental study of a hydrogenetic ferromanganese crust, from the Detroit Seamount using high-resolution magnetic and geochemical scanning. Our findings are as follows: (1) A total of 39 magnetozones are recognized in the studied section of the crust, which can be preliminarily correlated to the geomagnetic polarity timescale from chrons C1n to C5Dn. This correlation yields growth rates of 1.48–2.18 mm/ Myr over the past ~18 Myr. (2) Columnar and lamellar growth structures are identified with distinct metal enrichment patterns. A significant transition from lamellar to columnar growth occurred at ~11.6 Ma. (3) The quantified elements can be clustered into three groups, (Mn, Cu–Co–Ni, and Al–Si), (Fe and Ti), and Ca. A strong correlation between metal enrichment in the crust and the global benthic foraminifera $\delta^{13}C$ record is then observed. Based on these results, we suggest a predominant role of deep-sea redox conditions in the growth history of ferromanganese deposits on the Detroit Seamount since the Early Miocene.

1. Introduction

The Hawaiian Chain-Emperor Seamounts in the North Pacific (Fig. 1) consist of ~130 submarine volcanoes and extend over 6000 km. These seamounts can be used to track the motion of the Pacific Plate over the Hawaiian hotspot (Morgan, 1972; Wilson, 1963). It has been reported that the ages of these seamounts progressively increase from the Island of Hawaii to the Meiji Seamount (Clague and Dalrymple, 1989; Kerr et al., 2005), as a result of the northwestward movement of the Pacific Plate over the mantle hotspot at the Hawaii (e.g., Clague and Dalrymple, 1989; Tarduno et al., 2003).

Reconstructing the paleoposition of these seamounts is critical to explore how the Pacific Plate moved and the mantle behaved (e.g., Doubrovine and Tarduno, 2004; Sager, 2002). Several conclusions have been drawn (e.g., Koppers and Watts, 2010; Sun et al., 2021), although

they are not universally accepted. For example, the closure of the Neo-Tethys Ocean may have induced a major change (Sun et al., 2020) in the drifting direction of the Pacific Plate at the famous Hawaiian-Emperor chain bend (Morgan, 1972; Sharp and Clague, 2006; Wessel and Kroenke, 2009; Wilson, 1963). Towards the end of the Cretaceous, the plume/hotspot shifted southward, resulting in the current position, and the Emperor Seamounts underwent rapid migration prior to the middle Eocene (Tarduno et al., 2003, 2009).

The post-eruption history of these seamounts was relatively less documented, which could be attributed to that the infrequent coverage of the seafloor with detrital deposits. One of key materials for post-eruption studies are ferromanganese deposits (crust and nodule), and they contain a high concentration of critical metals, such as Mn, Cu, Co, and Ni, as well as platinum group elements and noble metals of mantle origin (e.g., Berezhnaya et al., 2021; Mikhailik et al., 2019; Mikhailik

et al., 2021). It has been suggested that Au in marine ferromanganese crusts (MFCs) could experience post-enrichment through hydrothermal fluid during rejuvenated volcanic stages (Mikhailik et al., 2021), while Pt would result from the halmirolysis of underlying basalts (Berezhnaya et al., 2021).

However, similar to studies conducted on ferromanganese deposits in other regions, there is a lack of direct comparison and overall consistency in time scales between metal enrichment and global climate changes. Although it has been recognized that abyssal erosion has occurred on a large scale and that ferromanganese deposits have developed in abundance since the late Oligocene as a result of the expansion of the Antarctic bottom water (Glasby, 1978; Kennett and Watkins, 1975), the role of global climate changes in the formation of ferromanganese deposits is not well understood unless a high-resolution age model is obtained (e.g., Chen et al., 2023; Yi et al., 2023). Hence, we conduct a study on a ferromanganese crust collected from the Detroit Seamount (Fig. 1) to investigate the external factor contributing to metal enrichment, using magnetic and X-ray fluorescence (XRF) scanning. By integrating precise dating and metal distribution in the crust, we aim to establish the long-term relationship between metal enrichment and climate changes during the Neogene-Quaternary period.

2. Materials and methods

2.1. Detroit Seamount

The Detroit Seamount locates at the northernmost end of the Hawaiian Chain-Emperor Seamounts, which was formed at about 76 Ma (Fig. 1). By integrating seismic data and ash layers in ODP Leg 197 sites, it is inferred that volcanic activity in the Detroit Seamount occurred during the Eocene and likely continued until the early Oligocene (Kerr et al., 2005). Since then, sediments were deposited and ferromanganese crusts developed on the seafloor.

2.2. The studied sample (SO249 DR65-6)

The studied ferromanganese crust was collected from the "Late stage" part of the Detroit Seamount during the SO249 cruise on June 29–30, 2016. The collection site was located at 50°32′N, 167°29′N, at a water depth of ~3000 m. The crust was obtained using a dredge track positioned at the base of the seamount, and the crust has dimensions of about 15 cm × 15 cm × 15 cm (Werner et al., 2016).

In the laboratory, the upper part (~32 mm) of the crust was sampled and polished for magnetic and XRF scanning in this study (Fig. 1).

Previous research has shown that vernadite is the major mineral in the studied sample, and the crust was formed through hydrogenetic processes without any hydrothermal influences (Mikhailik et al., 2023). Analysis of bulk samples indicates the following elemental contents: Si (14.3%), Al (2.95%), Ca (1.70%), Fe (20.2%), Ti (10.2%), Mn (0.64%), Co (1176 ppm), Cu (351 ppm), Ni (744 ppm), and rare earth elements (REE, 1529 ppm) (Mikhailik et al., 2023).

2.3. Magnetic scanning

Magnetic scanning was performed three times for the studied MFC (DR65-6) using a room-temperature Hall probe without demagnetization, following the procedure of Yi et al. (2020), at the State Key Laboratory of Marine Geology, Tongji University. These measurements produce high-resolution maps of the vertical component of the magnetic field (Yi et al., 2020), which can provide information on the micro-scale magnetic orientation within the sample (Kletetschka et al., 2013; Oda et al., 2011; Weiss et al., 2007). The room-temperature instrument employs a stationary axial Hall probe, equipped with a fiberglass tip sensor that is ~100 μm in size. The movement stage is an automated 2D motorized stage, enabling a spatial resolution of 1 μm.

The measurements were repeated 100 times, at 80 μm intervals along the same profile (A0). The magnetic sensor was positioned at a distance of 0.1 mm from the sample surface. The final magnetic signal was obtained as the average of the repeated scans. In order to ensure the reliability of the magnetic signals, two additional, parallel tracks (R1 and R2) to the major measuring line (A0) were obtained, with slight offsets of ±80 μm and repeated 50 times.

2.4. XRF mapping

In-situ elemental mapping for the studied MFC (DR65-6) was carried out by Micro-XRF instrument (Bruker, M4 Tornado) equipped with a poly-capillary lens-focused rhodium X-ray source and a Silicon Drift Detectors at the State Key Laboratory of Marine Geology, Tongji University. The Micro-XRF technique combines the advantages of an automated microscope-guided high-precision movable stage system with the spectral resolution of a high-energy X-ray source, enabling fast, non-destructive, and high-resolution elemental analysis (Beckhoff et al., 2007; Janssens, 2014). The Micro-XRF mapping was performed with a 50 kv X-ray tube voltage, 600 μA tube current, 30 μm step size and 10 ms dwell time/pixel. Nine elements, including Al, Si, Fe, Ti, Mn, Cu, Co, Ni, and Ca, were quantified in counts per second (cps).
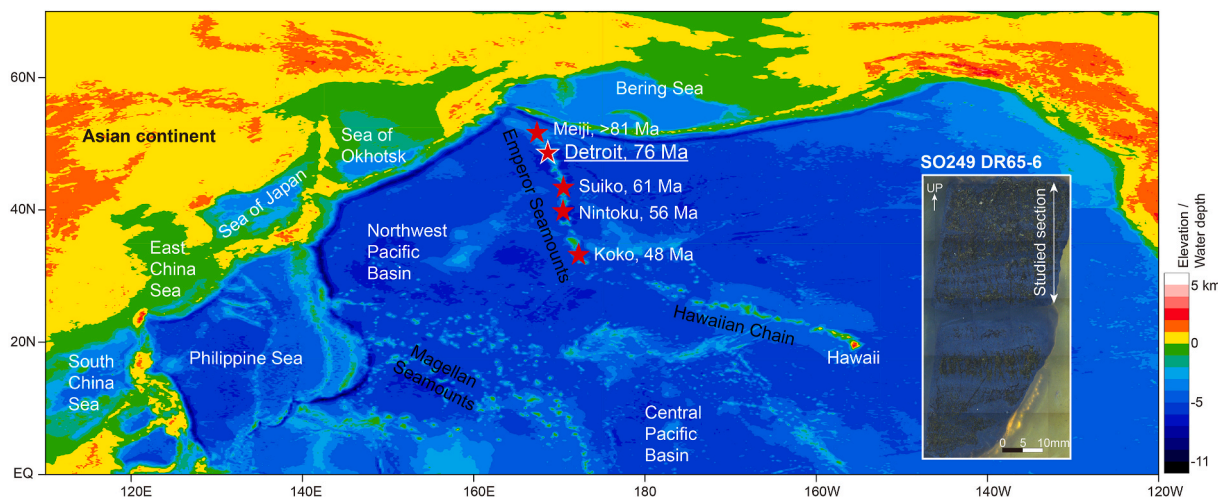

Fig. 1. Regional map of the North Pacific showing location of Detroit Seamount with the studied crust (DR65-6). The ages of the dated seamounts along the Emperor Chain are from Kerr et al. (2005).

3. Results and analysis

3.1. Magnetic signal and the age model

Magnetic scanning using a stationary Hall probe, repeated 100 times along the same profile line (A0), reveals a quasi-symmetrical and cyclical magnetic pattern of fluctuation (Fig. 2c). A comparable magnetic pattern can be replicated along the measuring lines (R1 and R2) away from the major profile (Fig. 2b and d), thereby validating the robustness of magnetic scanning.

In order to detect magnetic signals, we apply principal component analysis (PCA) to magnetic scanning data. The leading component accounts for 72.7% of the total variance (Line A0), and similar outputs are observed along the two reference lines (R1 and R2), explaining 64.1% and 64.9%, respectively. Subsequently, we utilize the leading components to represent changes in magnetic field of the studied MFC, and calculate the standard deviation between repeated scans as a measure of uncertainty in the magnetic signal (Fig. 2e).

A comparison was conducted to assess the reliability of magnetic scanning and the consistency between measuring lines (Fig. 2e). As a result, correlation coefficients between lines A0 and R1 and lines A0 and R2 are r = 0.62 ($p < 0.01$) and r = 0.52 ($p < 0.01$), respectively.

However, there are noticeable differences between the magnetic records along the three lines in certain intervals, such as 9–10 mm, 19–20 mm, 23–24 mm, and 30–31 mm (Fig. 2e). Two factors that could

contributed to these offsets are growth noisy and diachronous layering. Growth noisy is observed in magnetic signals within less compacted layers of a ferromanganese nodule in the Eastern Pacific, potentially due to a rapid-growing process (Yi et al., 2020). As for diachronous layering, coeval layers in a columnar structure of ferromanganese crusts are typically less developed compared to those in a lamellar structure. Since no other geochronological evidence was obtained in this study for cross-checking, these differences are treated as uncertainties in magnetic scanning. The record of magnetic field changes along the major profile (A0) was then used to identify potential geomagnetic reversals recorded in the studied crust (Fig. 2f).

With at least four continuous magnetic points, a total of 39 magnetozones are recognized (Fig. 3), including 20 normal zones (n01-n20) and 19 reverse zones (r01-r19). In order to establish chronological correlations, these magnetozones are firstly visually correlated to the geomagnetic polarity timescale 2020 (GPTS2020) (Gradstein et al., 2020) as commonly practiced in paleomagnetic research. The visual correlation primarily relies on the normal-reversed polarity pattern observed in DR65-6 magnetozones, assuming no major hiatus over millions of years. This correlation indicates that the studied section records chrons from C1n to C4Ar (Supplementary data), suggesting a ~10-Myr duration. This estimate closely aligns with previous $^{10}Be/^{9}Be$ results of ferromanganese deposits in this region (van de Flierdt et al., 2004b).

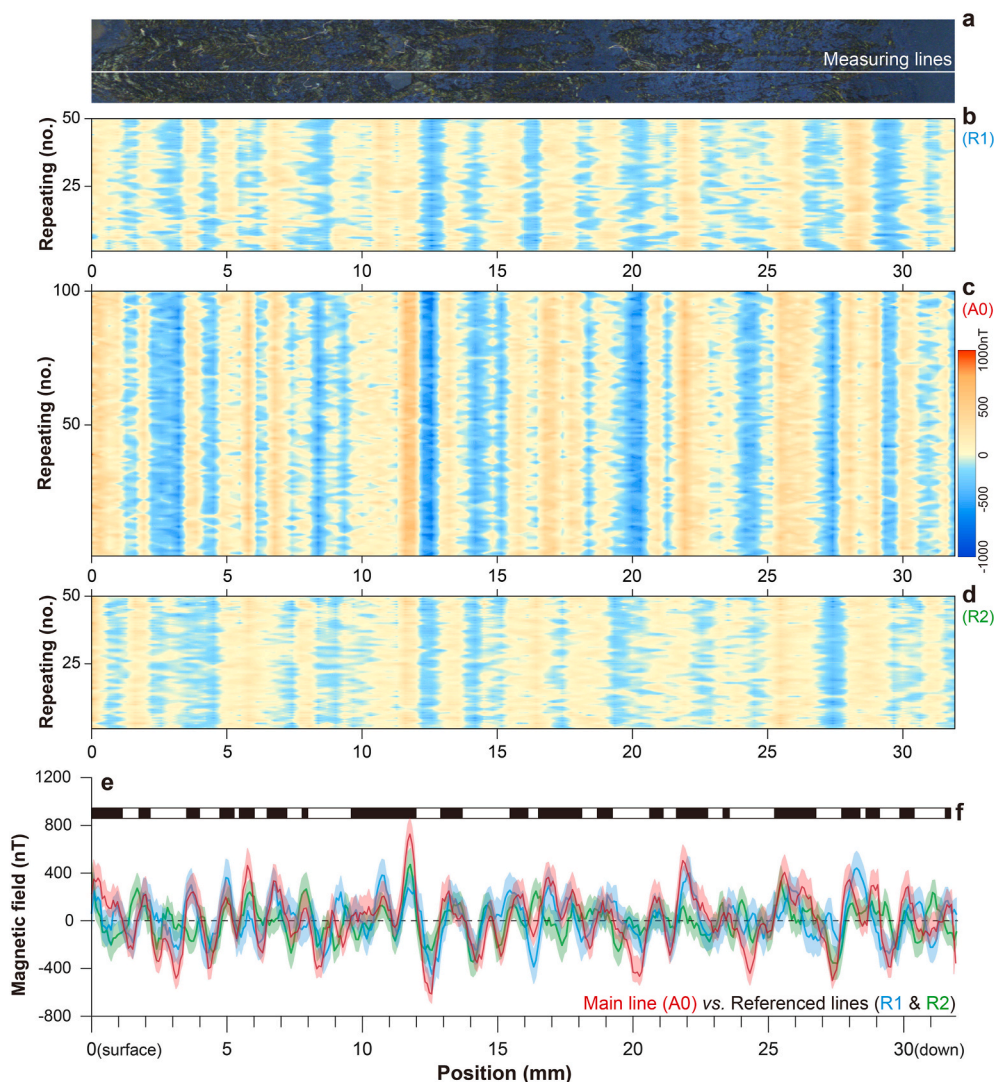Yet, when relying solely on long-term magnetostratigraphy without

Fig. 2. Magnetic signals by magnetic scanning of the studies MFC. (a) Image of the sampled crust marking out the measurement position for magnetic scanning. (b) and (d) Magnetic scans along 80 μm above (R1) and 80 μm below (R2) the major measuring line (A0), respectively. (c) Magnetic scans along the major measuring line (A0). (e) Comparison of changes in the magnetic field of the studied MFC with 68% confidence interval (shaded colors). The bold lines in (e) indicates the 5-point moving average of the original data. (f) The identified magnetozones; and see details in Fig. 3.
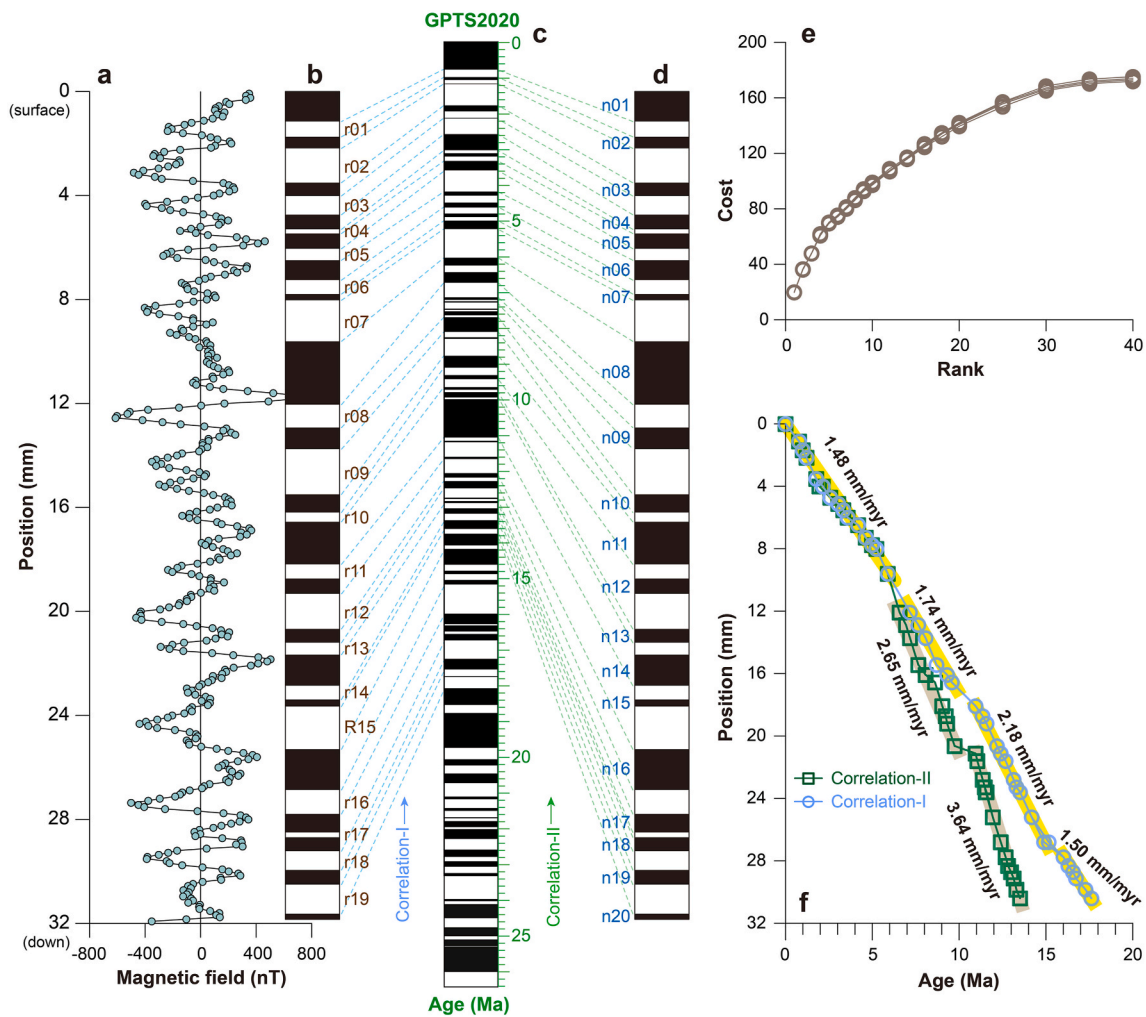
Fig. 3. Correlation of the identified magnetozones of the studied part of MFC DR65-6. (a) Changes in magnetic field by magnetic scanning along the major measuring line (A0 in Fig. 2). (b) and (d) The identified magnetozones. N01-n20, normal zones; r01-r19, reverse zones. (c) The geomagnetic polarity timescale (GPTS 2020) (Gradstein et al., 2020). (e) The cost-rank function for different numbers of magnetozones considered to evaluate the growth rate based upon the parameters chosen for this study. Parameters as set: load ref. From GPTS 2020, Nbr Res 100, Max path 1000–5000, Gap Factor 0, Max Subst 1–40 (since no substantial difference observed in changing Max path), Subst Dist 5. (f) Age-depth models for the studied MFC with the estimated growth rates. Correlation-I and Correlation-II represent the two scenarios of the magnetic correlations.

other geochronological evidence, the visual correlation of recorded magnetozones to the GPTS often results in inconsistencies (e.g., Qiao et al., 2016; Zhang et al., 2014). In order to minimize uncertainties in magnetic correlations, Lallier et al. (2013) developed a novel dynamic time warping algorithm technique to assess the reliability of different possibilities, providing valuable clarification (e.g., Zhang et al., 2017). By applying this new technique, two sets of magnetic correlations between DR65-6 magnetozones and the GPTS2020 are obtained, denoted as Correlation-I and Correlation-II (Supplementary data). These correlations were determined under the assumption that accumulation rates did not change abruptly and that thin magnetozones would not be correlated to long chrons (Lallier et al., 2013; Zhang et al., 2017). Upon adjusting the calculation parameters (Fig. 3e) as suggested by Zhang et al. (2017), Correlation-I remains valid, while Correlation-II is only supported when the Rank value is < 6. As a result, Correlation-II is excluded from subsequent analyses.

In terms of Correlation-I, chrons from C1n to C5Dn were recorded, while for Correlation-II, chrons from C1n to C5ABn were recorded. The discrepancy between these two correlations emerges at ~6 Ma, potentially indicating the influence of missing chrons. According to Correlation-I, the growth rates of the studied part of MFC DR65-6 exhibit noticeable variations, from 1.48 mm/Myr to 2.18 mm/Myr, suggesting

that the age of the bottom of the studied section (~32 mm) is about 17.6 Ma.

However, both correlations imply the studied section of MFC DR65-6 has a substantially longer duration, compared to regional estimates of ferromanganese deposits based on $^{10}Be/^9Be$ dating (van de Flierdt et al., 2004b). To confirm this correlation (Correlation-I), we compared the magnetic signal obtained from magnetic scans with various records of Earth's magnetic field, including changes in a ferromanganese nodule in the Eastern Pacific (Yi et al., 2020), seafloor magnetic anomalies in the South Atlantic (Li et al., 2018), marine magnetic anomalies in the Southern Hemisphere (Li et al., 2021), and relative paleomagnetic intensity (RPI) of IODP Site U1336 in the Equatorial Pacific (Ohneiser et al., 2013). As shown in Fig. 4, the comparisons reveal a consistent pattern of broad paleomagnetic field variations, and the relatively large difference shown in Fig. 4c may be attributed to the contamination of climatic signals in processing RPI data from deep-sea sediments (Guyodo et al., 2000; Roberts et al., 2003; Xuan and Channell, 2008). In addition, a similar relationship can be observed in an attempt of magnetic scanning of MFCs collected from the Northwest Pacific (Oda et al., 2011). It is thus inferred that the discrepancy between our estimates and previous $^{10}Be/^9Be$ dating in the Emperor Seamounts might be attributed to the specific location-based collection of ferromanganese deposits.
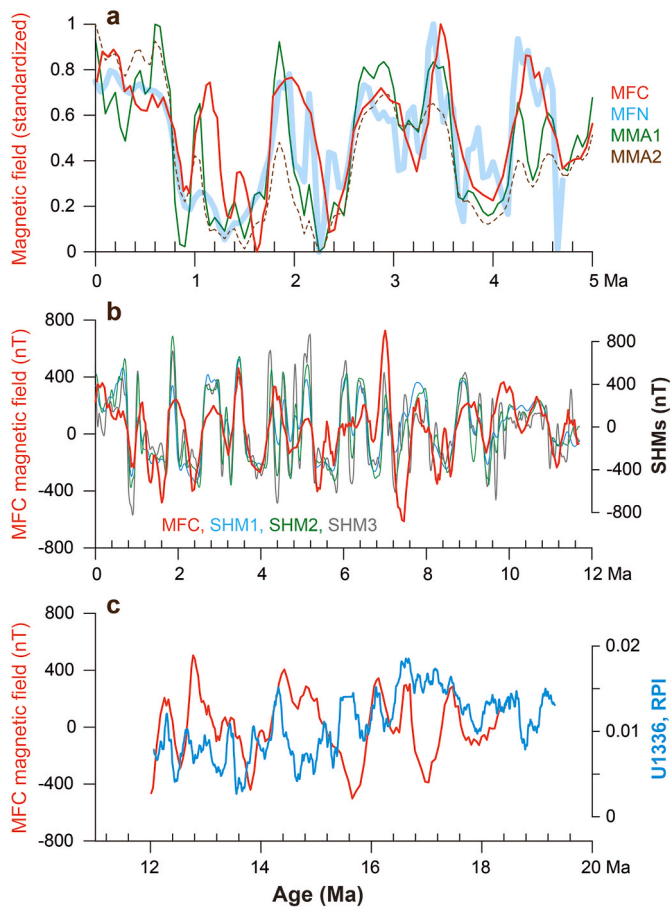
Fig. 4. Comparison of the magnetic signal of MFC DR65-6 with various records of relative paleomagnetic intensity (RPI). (a) Comparison over the past 5 Myr. MFC, this study. MFN, marine ferromanganese nodule (Yi et al., 2020). MMA1 and MMA2, seafloor magnetic anomaly and magnetization records of the South Atlantic, respectively (Li et al., 2018). (b) Comparison with the marine magnetic anomalies in the Southern Hemisphere (SHMs) (Li et al., 2021). (c) Comparison with the RPI record of IODP Site U1336 (Ohneiser et al., 2013).

Therefore, the reliability of DR65-6 geochronology has been verified, and this age model based on magnetic scanning (Correlation-I) is utilized for later analyses. For other possibilities of correlating magnetozones to the GPTS2020 (Supplementary data), they are still being considered in the light of new evidence in future.

3.2. Changes in metal elements

Generally, the studied part of MFC DR65-6 displays two distinct growth structure: (1) a columnar structure above ~22–23 mm and, (2) a lamellar structure observed below. The transition between these structures can be visually observed in elemental distributions (Fig. 5). Different structures may represent different mineralogy and metal enrichment, thus indicating different environmental conditions (e.g., Reykhard and Shulga, 2019). Specifically, the Mn distribution exhibits arborization-like patterns in the upper with lower values, and it displays laminated patterns in the lower with higher values. Conversely, the Fe accumulation pattern mirrors that of Mn, but with a contrary trend in contents. Element Ti exhibits a similar distribution to Fe, likely suggesting a potential association. However, elements Al and Si show no distinct changes in growth structure; instead, they are randomly enriched between layers or branches, consistent with previous findings (e.g., Hein et al., 2020; Yi et al., 2023). Elements Cu–Co–Ni (CCN) distribute no apparent pattern (Fig. 6a), likely due to their low concentrations in the crust. In addition, element Ca is enriched in the lower

laminated layers, without a clear pattern across the studied section.

Combining changes in various elements, the genesis can be identified (Fig. 6c), following the method of Bonatti et al. (1972). As shown, the XRF scanning points mainly reside in the hydrogenetic region, near the hydrogenetic-hydrothermal boundary. These observations are consistent with the results obtained from the bulk sample of MFC DR65-6 (Mikhailik et al., 2023), as well as with previous studies on crusts in this region (e.g., Berezhnaya et al., 2021; Mikhailik et al., 2019; Mikhailik et al., 2021).

Further analysis of the element contents confirms the relationship between elemental enrichment and growth structures (Figs. 7–8). For example, PCA results for the nine elements show three groups (Fig. 7a): Mn–Al–Si–CCN (PC1), Fe–Ti (PC2), and Ca. Detailed correlation analysis for paired elements supports this pattern (Fig. 8). As shown, the scatter plot between elements Mn and Fe reveals two clusters with different relationships (Fig. 7b), and these two clusters are also evident in the relationship between Mn and other elements (Fig. 8a–d). In contrary, the relationship between Fe and other elements is weak (Fig. 8e–g), except for element Ti (Fig. 8h), and no subgroup can be identified.

Various elements may be linked to different environmental processes. An example of this is the element Mn, which has been found to have a positive association with changes in dissolved oxygen (e.g., Hein et al., 2020; Skornyakova and Murdmaa, 1992; Yi et al., 2023). This can be attributed to the migration of oxygen-sensitive metals from reducing to oxidizing environments (Glasby, 2006). Another example is that the element Al has been found to represent terrigenous clast in the North Pacific, because it is closely associated with eolian dust in sediments (Uematsu et al., 1983) and in ferromanganese nodules (Yi et al., 2023). Changes in redox conditions and eolian inputs are both linked to global paleoenvironmental processes, such as orbital forcing and polar ice-sheet evolution in the past (Yi et al., 2023). However, unlike the distinct Fe–Mn relationships shown in Fig. 7b, a negative Fe–Mn relationship is expected in hydrogenetic crusts and nodules in the deep Pacific (e.g., Cheng et al., 2023; Ren et al., 2022; Ren et al., 2023). This negative relationship implies a competition between Fe and Mn, as depicted in the ternary diagram illustrating hydrothermal and hydrogenetic processes (Bonatti et al., 1972).

Integrating these results, the potential implications of the clustered elements are summarized as follows.

(1) For Mn–Al–Si–CCN (PC1), changes in Mn and CCN may be primarily influenced by redox conditions, whereas the dominant factor for Al and Si could be terrigenous input, such as ice-rafting and/or eolian debris. This group, in conjunction with the linkage between abyssal redox conditions and eolian dusts in the deep Pacific (Yi et al., 2023), indicates a potential common signal among various paleoclimatic processes. This is similar to the strong correlation observed between global foraminiferal $\delta^{18}O$ and $\delta^{13}C$ records (r = −0.80, p < 0.01).

(2) For Fe–Ti (PC-2), the subgroup with a negative Fe–Mn relation implies a hydrogenetic process in metal enrichment, consistent with findings from previous studies (e.g., Khanchuk et al., 2019; Mikhailik et al., 2013). Conversely, in the subgroup exhibiting a positive Fe–Mn relation, it is speculated that the presence of FeO_x could facilitate Mn(II) oxidation (Liu et al., 2022), potentially linking to an additional Fe source, within the context of similar minerals observed in different parts of MFC DR65-6 (Mikhailik et al., 2023).

(3) Ca is considered to be a relatively independent element that might have a correlation with marine productivity and/or the phosphatization effect (Koschinsky et al., 1997). Based on that there no significant variation observed in the contents of P and Ca in different parts of MFC DR65-6 (Mikhailik et al., 2023), it is inferred that the phosphatization effect can be disregarded in the past, and thus the element Ca was excluded in subsequent analyses.
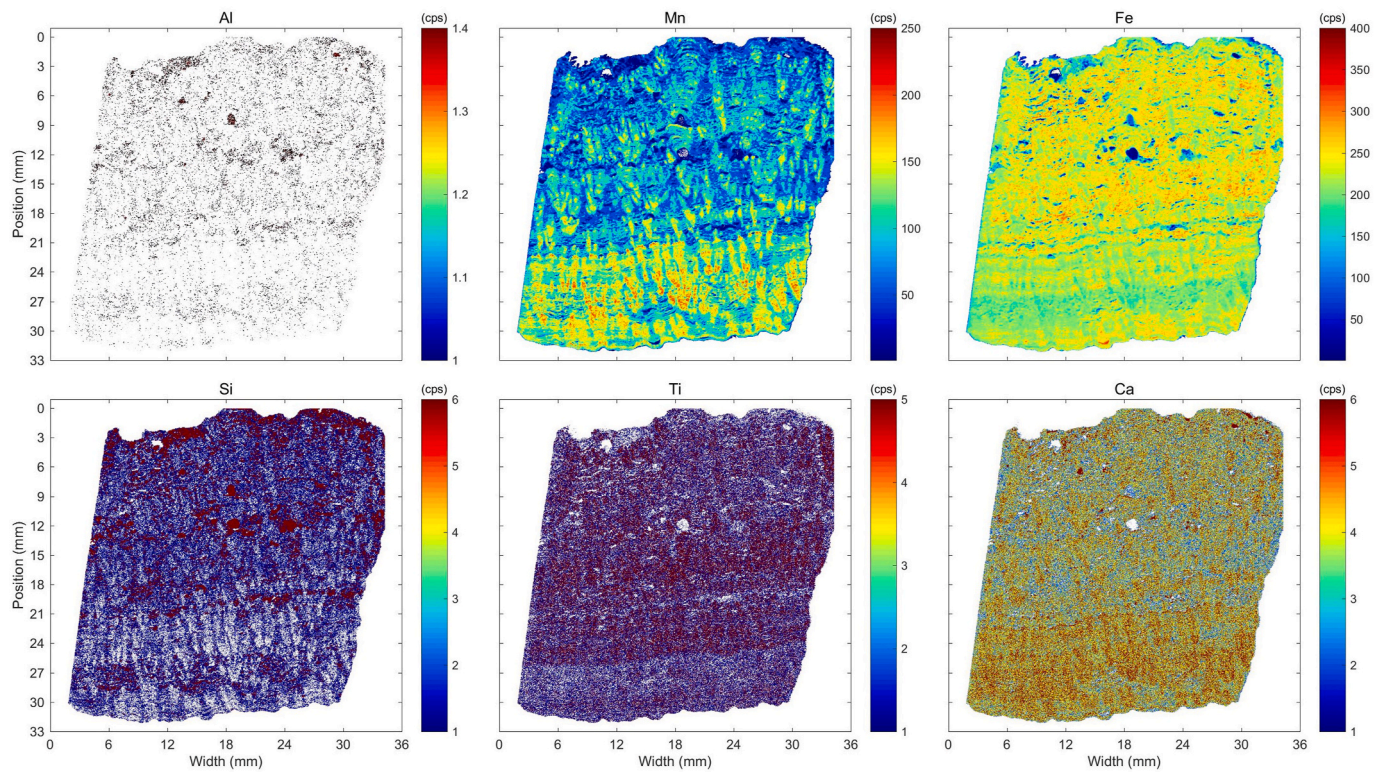
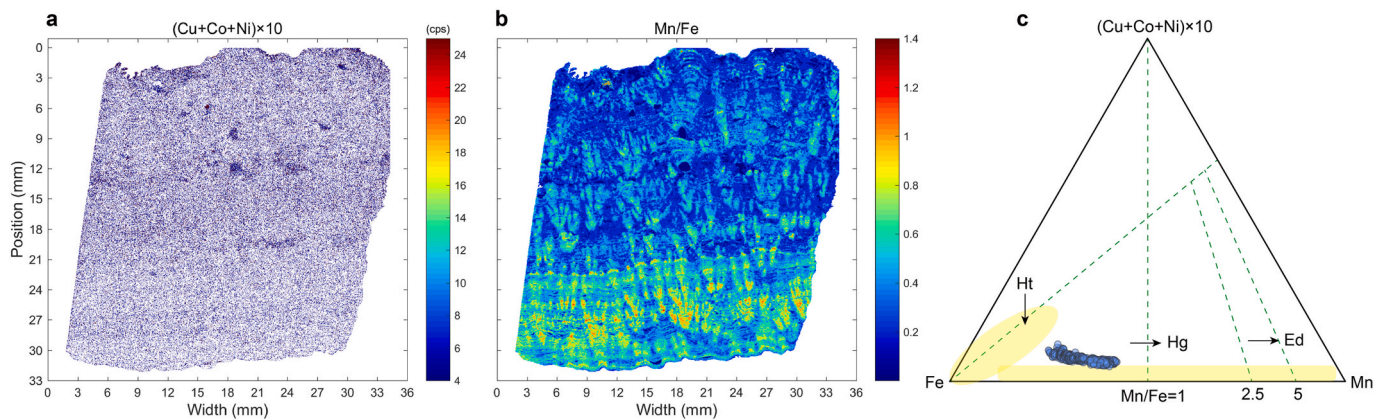**Fig. 5.** Element distribution of the studied part of MFC DR65-6.

Fig. 6. Growth type of the studied part of MFC DR65-6. Ternary diagram (right panel) of Fe, Mn, and (Cu + Co + Ni) × 10 is following Bonatti et al. (1972). The yellow-shaded area indicates the main influence of hydrothermal (Ht) process; Hg, hydrogenetic; Ed, early diagenetic.

4. Discussion

Previous studies have proposed that the formation of ferromanganese deposits on the deep-sea floor are closely related to the migration of manganese and other critical metals (Glasby, 2006). This is because these metals are typically dissolved from the oxygen-minimum zone (OMZ) and the oxidized environment below the OMZ promotes the formation of metal oxides (Halbach et al., 2017). The growth of these deposits is very slow, usually <1 cm/Myr, and is influenced by long-term environmental changes, such as bottom-water evolution (e.g., van de Flierdt et al., 2004a) and terrestrial dust supply (e.g., Banakar et al., 2003). However, the broad consistency between changes in critical metals in ferromanganese deposits and climatic proxies of global/-regional change, such as marine foraminiferal isotopes ($\delta^{18}O$ and $\delta^{13}C$), has been less reported, making it unclear what external factors drive metal enrichment (Guan et al., 2019; Manceau et al., 2014; Yi et al.,

2023). One limitation is lack of precise dating. Current dating techniques, including U–Th series (Ku, 1976), $^{10}Be/^{9}Be$ (Graham et al., 2004), Co flux (e.g., Puteanus and Halbach, 1988), $^{87}Sr/^{86}Sr$ (Richter and Turekian, 1993), and $^{187}Os/^{188}Os$ (Klemm et al., 2005), usually enable age models for researches only on long timescales (tens of millions of years) (e.g., Halbach et al., 2017; Hein et al., 2013; Hein et al., 2015; Ren et al., 2023; van de Flierdt et al., 2004a; Wegorzewski and Kuhn, 2014; Zhong et al., 2021).

Constrained by magnetic scanning (Fig. 3) and by averaging metal data obtained from each position in XRF mapping (Figs. 5–6), the metal variations in the studied part of MFC DR65-6 exhibit a strong correlation with the deep-sea stacked $\delta^{18}O$ and $\delta^{13}C$ records (Figs. 9–10). This provides an opportunity to testify the potential role of global climate changes in metal enrichment in the Detroit Seamount.

The stable carbon isotope ($\delta^{13}C$) is a powerful and broad-used proxy in paleoceanography (e.g., Mackensen and Schmiedl, 2019; Shackleton
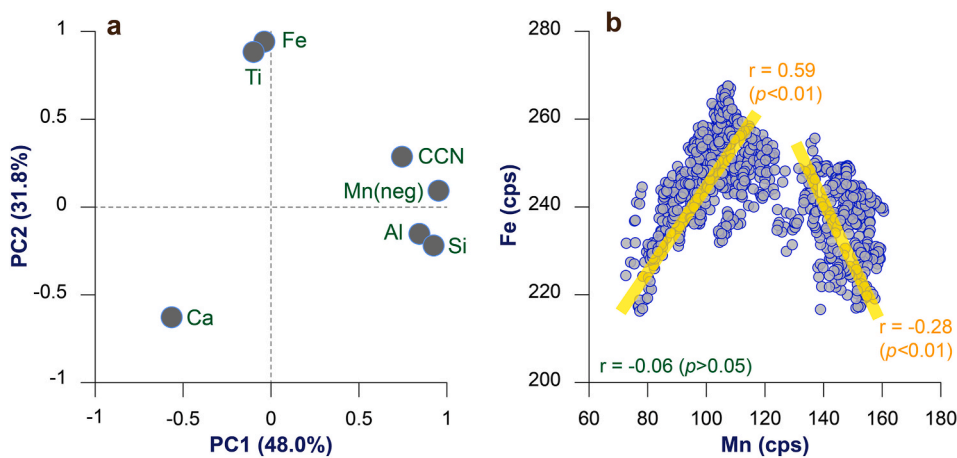
Fig. 7. Scatter plots between PC1 and PC2 (a) and between Mn and Fe (b). PC1 and PC2, the two extracted components from principal component analysis (PCA), and 48.0% and 31.8% are two variance values of PC1 and PC2, respectively. CCN, Co + Cu + Ni; Mn (neg), all data of element Mn are transferred to negative values for PCA. Correlation coefficients (r) with their significance levels are labeled. There are two subgroups identified in (b), and the boundary between them is dated to ~11.6 Ma.
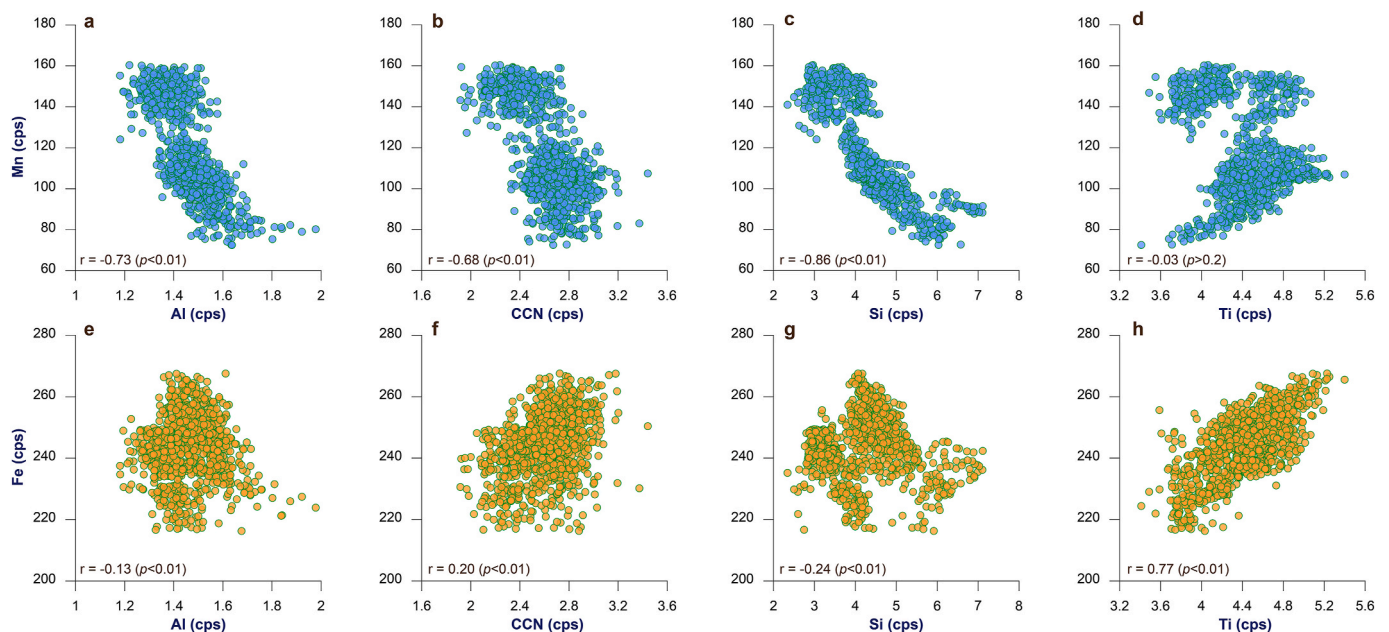

Fig. 8. Scatter plots between paired elements of the studied part of MFC DR65-6. CCN, Co + Cu + Ni; Correlation coefficients (r) with their significance levels are labeled.

and Opdyke, 1977; Curry and Oppo, 2005), which could be influenced by a series of factors, including carbon dioxide, methane and oceanic dissolved carbons (e.g., Barnola et al., 1987; Broecker and Peng, 1993; Glibert et al., 2019; Kroopnick, 1974; Veizer et al., 1999; Zeebe, 2007). For long-term variation, the benthic $\delta^{13}C$ record is indicative of oceanic alkalinity or the balance between dissolved inorganic carbon (DIC) and alkalinity (Zachos et al., 2001). Because of this and together with that different water masses are known to have distinct $\delta^{13}C$ values (e.g., Mackensen and Schmiedl, 2019), the benthic $\delta^{13}C$ record has been employed as a proxy of deep-sea ventilation (e.g., Eide et al., 2017; Hodell and Venz-Curtis, 2006; Hodell et al., 2003).

Considering that the main trend shown in the benthic $\delta^{13}C$ record and other ventilation proxies is generally similar during the Neogene-Quaternary period (Auderset et al., 2022; Hess et al., 2023; Zachos et al., 2001), we suggest that the high correlation (r = 0.83, $p < 0.01$) between Mn, Mn/Fe, and the benthic $\delta^{13}C$ record (Westerhold et al., 2020) indicates that redox conditions may have played a predominant role in metal enrichment at the site (Fig. 9a and b). In turn, high Mn and Mn/Fe values are indicative of enhanced ventilation and high dissolved oxygen, consistent with a recent finding from a ferromanganese nodule

in the Eastern Pacific (Yi et al., 2023). Nevertheless, certain differences between our Mn records and the benthic $\delta^{13}C$ record are also observed in the past ~18 Myr, inferring those other factors (Halbach et al., 2017; Hein et al., 2020), such as marine productivity, metal supply, porewater conditions, and/or terrigenous input, could have influences on metal enrichment, which is worthy of clarification in future.

Moreover, the benthic $\delta^{18}O$ record can serve as a proxy for global temperature (e.g., Zachos et al., 2001), generally reflecting the evolution of ice sheets in the high-latitude region of the Northern Hemisphere. The Northern Hemisphere glaciation has played a dominant role in the aridification processes in inner Asia (An et al., 2001; Guo et al., 2002) and the transport of eolian dust to the North Pacific (Rea, 1994; Rea and Hovan, 1995). Given the location of our study area (50°32′N, 167°29′N), we expect that terrigenous inputs are linked to changes in ice-rafting and/or eolian debris. Based on the observed covariation between marine foraminiferal isotopes (r = −0.80, $p < 0.01$) (Westerhold et al., 2020), we confirm that the clustered elements, including Mn–Al–Si–CCN (PC1), likely represent a common signal between the $\delta^{18}O$ and $\delta^{13}C$ records (Fig. 9c). Additionally, the time of the transition between the two growth structures (Figs. 5–6) and the change in Mn–Fe relationships
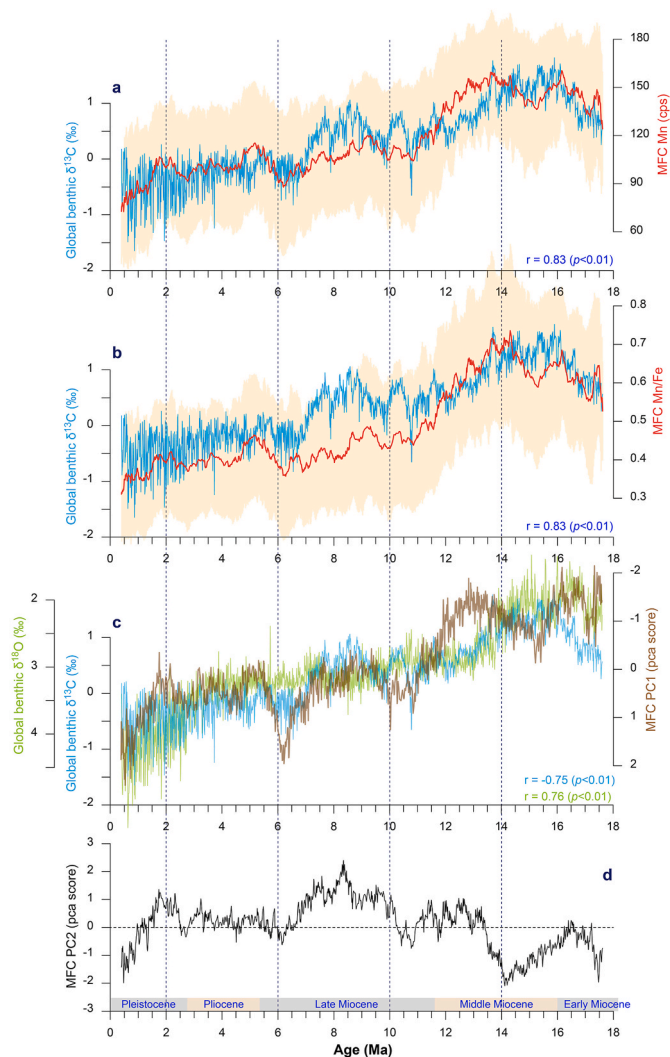
Fig. 9. Comparison between element accumulation of the studied part of MFC DR65-6 and global benthic δ^{13}C and δ^{18}O records (Westerhold et al., 2020). The shaded regions in (a–b) indicate 68% confidence interval of MFC proxies. The correlation coefficient between PC1 and the common signal of δ^{13}C and δ^{18}O is r = −0.79 ($p < 0.01$).

(Fig. 7b) corresponds well with the shift in the relationship between the δ^{18}O and δ^{13}C records at ~11.6 Ma (Westerhold et al., 2020). Therefore, we hypothesized that the interaction between global temperature and oceanic redox conditions (inferred from changes in alkalinity and DIC) may be a crucial factor in determining the growth types/structures in ferromanganese crusts, as well as the behaviors of metals, such as CCN and others.

Changes in the relationship between these proxies confirm a major shift at ~11.6 Ma (Fig. 10). Prior to ~11.6 Ma, the DR65-6 crust exhibits lamellar structures with higher Mn levels, higher Mn/Fe ratios, a negative correlation between Mn and Fe, lower Al and Si inputs, and a weak correlation with changes in oceanic alkalinity (DIC). Since ~11.6 Ma, an opposite pattern is observed within columnar structures. Different growth processes may lead to different metal behaviors (e.g., Li et al., 2020; Manceau et al., 2014; Reykhard and Shulga, 2019), and revealing the climatic context could potentially help distinguish the driving mechanisms behind different growth processes in future.

In addition, considering that the study area is recognized as one of the most active hotspot regions on Earth, where deep-hydrothermal materials were leaked into seawater (e.g., Koppers and Watts, 2010), the additional Fe source contributing to the positive Fe–Mn relationship in the upper part of MFC DR65-6 might be associated with hydrothermal materials. This is supported by the ternary diagram (Fig. 6c), which suggests an enrichment of Fe that is characteristic of hydrothermal processes (Bonatti et al., 1972). As a potential proxy of the supply of hydrothermal materials, changes in Fe–Ti (PC2) display a ~4-Myr oscillation (Fig. 9d). However, in this study, we do not consider this cyclic pattern as evidence of periodic leakage of mantle materials in the Detroit Seamount, due to the presence of a hydrogenetic sources of Fe and Ti in significant amounts (e.g., Khanchuk et al., 2019; Mikhailik et al., 2013, 2023), as well as potential interference from other metals in a PCA process. Despite these considerations, the relatively high variability of PC2 since ~13 Ma might indicate an active condition during the post-eruption phase in the study area, resulting in the increased inputs of Fe and Ti, leading to the accumulation of Mn and other metals. This may explain the positive Fe–Mn relationship (Fig. 7b), which is atypical of hydrogenetic processes. Moreover, the active post-eruption condition may also suggest that the influence of the metal supply on metal enrichment was not measurable. Therefore, we propose that global climate changes are the primary factor dominating the growth of ferromanganese crusts on the Detroit Seamounts, with a noticeable hydrothermal influence that cannot be overlooked.

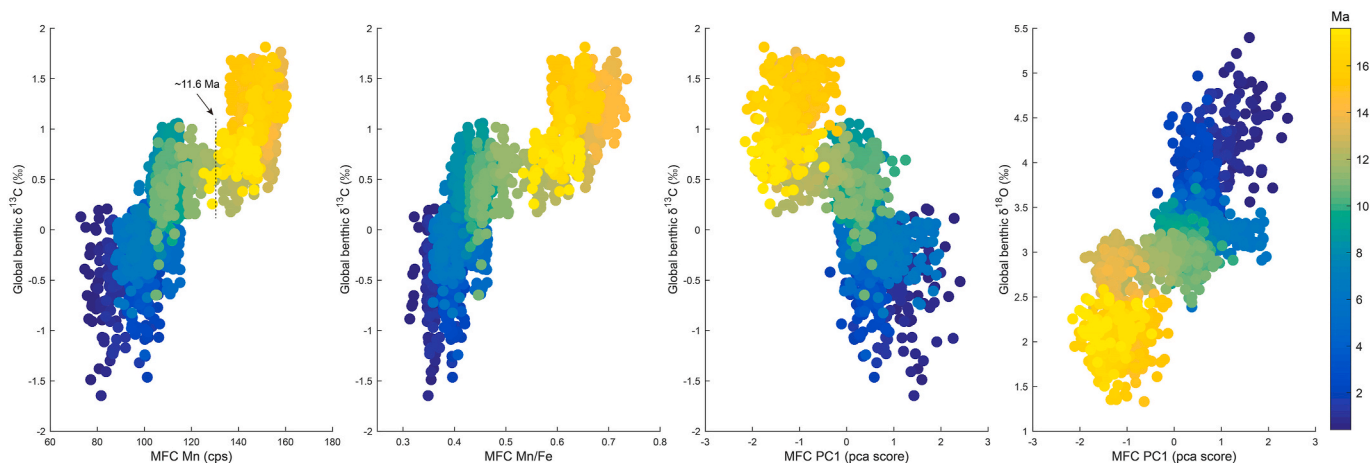**Fig. 10.** Scatter plots between element accumulation of the studied part of MFC DR65-6 and global benthic δ^{13}C and δ^{18}O records (Westerhold et al., 2020). Ages are shown in different colors. There are two subgroups identified in (a–c), same as Fig. 7b, and the boundary between them is dated to ~11.6 Ma.

5. Conclusions

We conducted an investigation on a ferromanganese crust collected from the Detroit Seamount in terms of geochronology and geochemistry. The aim was to understand the long-term association between metal enrichment in ferromanganese crusts on the Emperor Seamounts and global climate changes. The main findings are as follows: 1) Employing high-resolution magnetic scanning, we successfully established an age-growth model, which reveals estimated growth rates of 1.48–2.18 mm/Myr in the past ~18 Myr. 2) Micro-XRF mapping allowed us to identify two distinct growth structures, namely columnar and lamellar, each displaying unique metal enrichment patterns. 3) We observed three groups of metal behavior, including (Mn, Cu–Co–Ni, and Al–Si), (Fe and Ti), and relative independent Ca. By Integrating these findings, we found a strong correlation between metal enrichment and changes in oceanic alkalinity, notably influenced by hydrothermal materials. Consequently, we conclude that global climate changes, specifically deep-sea redox conditions, are the predominant drivers of the growth processes in the ferromanganese crusts at the site since the Early Miocene.

Author contributions

Conceptualization and methodology, L.Y.; sample collection, P.M.; formal analysis, L.Y., Y.L., P.M., and Y.Q.; Writing – original draft, L.Y.; Writing – review & editing, L.Y., and C.D. All authors contributed to the data interpretation and the final manuscript.

Data availability

All data support the findings of this study are available in an online repository (https://mda.vliz.be/print.php?file=VLIZ_00000824_63f 33195d2af9767595227).

Declaration of competing interest

The authors declare that they have no known competing financial interests or personal relationships that could have appeared to influence the work reported in this paper.

Acknowledgements

Appendix B. Supplementary data

Supplementary data to this article can be found online at https://doi.org/10.1016/j.quaint.2023.08.002.

References

Banakar, V.K., Galy, A., Sukumaran, N.P., Parthiban, G., Volvaiker, A.Y., 2003. Himalayan sedimentary pulses recorded by silicate detritus within a ferromanganese crust from the Central Indian Ocean. Earth Planet Sci. Lett. 205, 337–348.

Barnola, J.M., Raynaud, D., Korotkevich, Y.S., Lorius, C., 1987. Vostok ice core provides 160,000-year record of atmospheric CO_2. Nature 329, 408–414.

Beckhoff, B., Kanngießer, h.B., Langhoff, N., Wedell, R., Wolff, H., 2007. Handbook of Practical X-Ray Fluorescence Analysis. Springer Berlin, Heidelberg.

Berezhnaya, E.D., Dubinin, A.V., Zologina, E.N., Mikhailik, E.V., 2021. Platinum group element geochemistry in ferromanganese crust of the Detroit guyot, pacific ocean. Oceanology 61, 94–103.

Bonatti, E., Kraemer, T., Rydell, H., 1972. Classification and genesis of submarine ironmanganese deposits. In: Horn, D.R. (Ed.), Ferromanganese Deposits on the Ocean Floor. NSF, US, Washington D.C., pp. 149–166

Broecker, W.S., Peng, T.-H., 1993. Evaluation of the ^{13}C constraint on the uptake of fossil fuel CO_2 by the ocean. Global Biogeochem. Cycles 7, 619–626.

Chen, T., Zheng, J., Li, T., Shi, X., Robinson, L.F., Wang, M., Li, G., Ling, H., Ren, X., Ji, J., 2023. Thorium isotope evidence for glacial-interglacial dust storminess and productivity in the North Pacific gyre. Geochem. Cosmochim. Acta 346, 15–28.

Cheng, Y., Xu, Y., Yi, L., Li, D., Lin, F., Yin, X., Wang, A., 2023. Chronology and critical metals enrichment mechanism of ferromanganese nodules from the Parece Vela Basin, Philippine Sea. Chem. Geol. 630, 121494.

Clague, D.A., Dalrymple, G.B., 1989. Tectonics, geochronology, and origin of the Hawaiian-Emperor volcanic chain. In: Winterer, E.L., Decker, R.W., Hussong, D.M. (Eds.), The Geology of North America, Vol. N, the Eastern Pacific Ocean and Hawaii,. The Geological Sociaty of America, Boulder, CO, pp. 188–197.

Curry, W.B., Oppo, D.W., 2005. Glacial water mass geometry and the distribution of $\delta^{13}C$ of ΣCO_2 in the western Atlantic Ocean. Paleoceanography 20, PA1017.

Doubrovine, P.V., Tarduno, J.A., 2004. Late cretaceous paleolatitude of the Hawaiian hot spot: new paleomagnetic data from Detroit seamount (ODP site 883). G-cubed 5, Q11L04.

Eide, M., Olsen, A., Ninnemann, U.S., Johannessen, T., 2017. A global ocean climatology of preindustrial and modern ocean $\delta^{13}C$. Global Biogeochem. Cycles 31, 515–534.

Glasby, G.P., 1978. Deep-sea manganese nodules in the stratigraphic record: evidence from DSDP cores. Mar. Geol. 28, 51–64.

Glasby, G.P., 2006. Manganese: predominant role of nodules and crusts. In: Schulz, H.D., Zabel, M. (Eds.), Marine Geochemistry. Springer Berlin Heidelberg, Berlin, Heidelberg, pp. 371–427.

Glibert, P.M., Middelburg, J.J., McClelland, J.W., Jake Vander Zanden, M., 2019. Stable isotope tracers: enriching our perspectives and questions on sources, fates, rates, and pathways of major elements in aquatic systems. Limnol. Oceanogr. 64, 950–981.

Gradstein, F.M., Ogg, J.G., Schmitz, M.D., Ogg, G.M., 2020. Geologic Time Scale 2020. Elsevier.

Graham, I.J., Carter, R.M., Ditchburn, R.G., Zondervan, A., 2004. Chronostratigraphy of ODP 181, Site 1121 sediment core (Southwest Pacific Ocean), using $^{10}Be/^9Be$ dating of entrapped ferromanganese nodules. Mar. Geol. 205, 227–247.

Guan, Y., Ren, Y., Sun, X., Xiao, Z., Wu, Z., Liao, J., Guo, Z., Wang, Y., Huang, Y., 2019. Fine scale study of major and trace elements in the Fe-Mn nodules from the South China Sea and their metallogenic constraints. Mar. Geol. 416, 105978.

Guo, Z., Ruddiman, W.F., Hao, Q., Wu, H., Qiao, Y., Zhu, R., Peng, S., Wei, J.J., Yuan, B., Liu, T.S., 2002. Onset of Asian desertification by 22 Myr ago inferred from loess deposits in China. Nature 416, 159–163.

Guyodo, Y., Gaillot, P., Channell, J.E.T., 2000. Wavelet analysis of relative geomagnetic paleointensity at ODP Site 983. Earth Planet Sci. Lett. 184, 109–123.

Halbach, P.E., Jahn, A., Cherkashov, G., 2017. Marine Co-rich ferromanganese crust deposits: description and formation, occurrences and distribution, estimated world-wide resources. In: Sharma, R. (Ed.), Deep-Sea Mining: Resource Potential, Technical and Environmental Considerations. Springer International Publishing, Cham, pp. 65–141.

Hein, J.R., Koschinsky, A., Kuhn, T., 2020. Deep-ocean polymetallic nodules as a resource for critical materials. Nat. Rev. Earth Environ. 1, 158–169.

Hein, J.R., Mizell, K., Koschinsky, A., Conrad, T.A., 2013. Deep-ocean mineral deposits as a source of critical metals for high- and green-technology applications: comparison with land-based resources. Ore Geol. Rev. 51, 1–14.

Hein, J.R., Spinardi, F., Okamoto, N., Mizell, K., Thorburn, D., Tawake, A., 2015. Critical metals in manganese nodules from the Cook Islands EEZ, abundances and distributions. Ore Geol. Rev. 68, 97–116.

Hess, A.V., Auderset, A., Rosenthal, Y., Miller, K.G., Zhou, X., Sigman, D.M., Martínez-García, A., 2023. A well-oxygenated eastern tropical Pacific during the warm Miocene. Nature. https://doi.org/10.1038/s41586-023-06104-6.

Hodell, D.A., Venz-Curtis, K.A., 2006. Late Neogene history of deepwater ventilation in the southern ocean. G-cubed 7, Q09001.

Hodell, D.A., Venz, K.A., Charles, C.D., Ninnemann, U.S., 2003. Pleistocene vertical carbon isotope and carbonate gradients in the South Atlantic sector of the Southern Ocean. G-cubed 4, 1–19.

Janssens, K., 2014. X-ray fluorescence analysis. In: Gauglitz, G., Moore, D.S. (Eds.), Handbook of Spectroscopy. Wiley-VCH, Weinheim, Germany, pp. 449–506.

Kennett, J.P., Watkins, N.D., 1975. Deep-Sea erosion and manganese nodule development in the southeast Indian ocean. Science 188, 1011–1013.

Kerr, B.C., Scholl, D.W., Klemperer, S.L., 2005. Seismic stratigraphy of Detroit Seamount, Hawaiian-Emperor seamount chain: post-hot-spot shield-building volcanism and deposition of the Meiji drift. G-cubed 6, Q07L10.

Khanchuk, A.I., Mikhailik, P.E., Mikhailik, E.V., 2019. Distribution Ti in Mineral Fractions of Ferromanganese Deposits From the N-W Pacific. IOP Conference Series: Earth and Environ. Sci. 272, 022224.

Klemm, V., Levasseur, S., Frank, M., Hein, J.R., Halliday, A.N., 2005. Osmium isotope stratigraphy of a marine ferromanganese crust. Earth Planet Sci. Lett. 238, 42–48.

An, Z., Kutzbach, J.E., Prell, W.L., Porter, S.C., 2001. Evolution of Asian monsoons and phased uplift of the Himalaya-Tibetan plateau since Late Miocene times. Nature 411, 62–66.

Auderset, A., Moretti, S., Taphorn, B., Ebner, P.-R., Kast, E., Wang, X.T., Schiebel, R., Sigman, D.M., Haug, G.H., Martínez-García, A., 2022. Enhanced ocean oxygenation during Cenozoic warm periods. Nature 609, 77–82.

Kletetschka, G., Schnabl, P., Šifnerová, K., Tasáryová, Z., Manda, Š., Pruner, P., 2013. Magnetic scanning and interpretation of paleomagnetic data from Prague Synform's volcanics. Studia Geophys. Geod. 57, 103–117.

Koppers, A.A.P., Watts, A.B., 2010. Intraplate seamounts as a window into deep earth processes. Oceanography 23, 42–57.

Koschinsky, A., Stascheit, A., Bau, M., Halbach, P., 1997. Effects of phosphatization on the geochemical and mineralogical composition of marine ferromanganese crusts. Geochem. Cosmochim. Acta 61, 4079–4094.

Kroopnick, P., 1974. The dissolved O_2-CO_2-^{13}C system in the eastern equatorial pacific. Deep Sea Res. Oceanogr. Abstr. 21, 211–227.

Ku, T.L., 1976. The uranium-series methods of age determination. Annu. Rev. Earth Planet Sci. 4, 347–379.

Lallier, F., Antoine, C., Charreau, J., Caumon, G., Ruiu, J., 2013. Management of ambiguities in magnetostratigraphic correlation. Earth Planet Sci. Lett. 371–372, 26–36.

Li, D., Fu, Y., Sun, X., Wei, Z., 2020. Critical metal enrichment mechanism of deep-sea hydrogenetic nodules: insights from mineralogy and element mobility. Ore Geol. Rev. 118, 103371.

Li, Y., Liu, J., Liu, Q., 2021. Geomagnetic field paleointensity spanning the past 11 Myr from marine magnetic anomalies in the southern Hemisphere. Geophys. Res. Lett. 48, e2021GL093235.

Li, Y., Liu, Q.-S., Wei, D., Li, S., Yu, Y., 2018. Variations of earth magnetic field intensity for the past 5 Myr derived from marine magnetic anomalies in a slowly spreading South Atlantic ridge. J. Geophys. Res. Solid Earth 123, 7321–7337.

Liu, J., Chen, Q., Yang, Y., Wei, H., Laipan, M., Zhu, R., He, H., Hochella, M.F., 2022. Coupled redox cycling of Fe and Mn in the environment: the complex interplay of solution species with Fe- and Mn-(oxyhydr)oxide crystallization and transformation. Earth Sci. Rev. 232, 104105.

Mackensen, A., Schmiedl, G., 2019. Stable carbon isotopes in paleoceanography: atmosphere, oceans, and sediments. Earth Sci. Rev. 197, 102893.

Manceau, A., Lanson, M., Takahashi, Y., 2014. Mineralogy and crystal chemistry of Mn, Fe, Co, Ni, and Cu in a deep-sea Pacific polymetallic nodule. Am. Mineral. 99, 2068–2083.

Mikhailik, P., Khanchuk, A., Mikhailik, E., Zarubina, N., Blokhin, M., 2019. Compositional variations and genesis of sandy-gravel ferromanganese deposits from the yōmei guyot (holes 431, 431A DSDP), emperor ridge. Minerals 9, 709.

Mikhailik, E.V., Khanchuk, A.I., Mikhailik, P.E., Barinov, N.N., Zarubina, N.V., 2013. The first find of visible gold in ferromanganese crusts of the Pacific Ocean. Doklady Earth Sci. 449, 422–426.

Mikhailik, P., Khanchuk, A.I., Mikhailik, E., Rashidov, V.A., Savelyev, D.P., Zarubina, N. V., 2023. Ferromanganese deposits of the North Pacific ocean. Russian J. Pacific Geol. 17, 101–133.

Mikhailik, P., Mikhailik, E., Ivanov, V., 2021. Gold in ferromanganese deposits from the NW pacific. Minerals 11, 979.

Morgan, W.J., 1972. Deep mantle convection plumes and plate motions. AAPG (Am. Assoc. Pet. Geol.) Bull. 56, 203–213.

Oda, H., Usui, A., Miyagi, I., Joshima, M., Weiss, B.P., Shantz, C., Fong, L.E., McBride, K. K., Harder, R., Baudenbacher, F.J., 2011. Ultrafine-scale magnetostratigraphy of marine ferromanganese crust. Geology 39, 227–230.

Ohneiser, C., Acton, G., Channell, J.E.T., Wilson, G.S., Yamamoto, Y., Yamazaki, T., 2013. A middle Miocene relative paleointensity record from the Equatorial Pacific. Earth Planet Sci. Lett. 374, 227–238.

Puteanus, D., Halbach, P., 1988. Correlation of Co concentration and growth rate - a method for age determination of ferromanganese crusts. Chem. Geol. 69, 73–85.

Qiao, Q., Huang, B., Piper, J.D.A., 2016. Tectonophysics, 2014. In: Zhang, Tao, Fang, Xiaomin, Chunhui Song, Appel, Erwin, Wang, Yadong (Eds.), Comment on "Cenozoic Tectonic Deformation and Uplift of the South Tian Shan: Implications from Magnetostratigraphy and Balanced Cross-Section Restoration of the Kuqa Depression, vol. 690, pp. 362–366. https://doi.org/10.1016/j.tecto.2014.04.044. Tectonophysics.

Rea, D.K., 1994. The paleoclimatic record provided by eolian deposition in the deep sea: the geologic history of wind. Rev. Geophys. 32, 159–195.

Rea, D.K., Hovan, S.A., 1995. Grain size distribution and depositional processes of the mineral component of abyssal sediments: lessons from the North Pacific. Paleoceanography 10, 251–258.

Ren, J., He, G., Deng, X., Deng, X., Yang, Y., Yao, H., Yang, S., 2022. Metallogenesis of Co-rich ferromanganese nodules in the northwestern Pacific: selective enrichment of metallic elements from seawater. Ore Geol. Rev. 143, 104778.

Ren, J., Yao, H., Yang, Y., Wang, L., He, G., Lai, P., Zhou, J., Deng, X., Liu, S., Deng, X., Jiang, Y., 2023. Critical metal enrichment in atypical hydrogenetic ferromanganese nodules: a case study in the Central Basin Ridge of the West Philippine Basin. Chem. Geol. 615, 121224.

Reykhard, L.Y., Shulga, N.A., 2019. Fe-Mn nodule morphotypes from the NE clarion-clipperton fracture zone, pacific ocean: comparison of mineralogy, geochemistry and genesis. Ore Geol. Rev. 110, 102933.

Richter, F.M., Turekian, K.K., 1993. Simple models for the geochemical response of the ocean to climatic and tectonic forcing. Earth Planet Sci. Lett. 119, 121–131.

Roberts, A.P., Winklhofer, M., Liang, W.-T., Horng, C.-S., 2003. Testing the hypothesis of orbital (eccentricity) influence on Earth's magnetic field. Earth Planet Sci. Lett. 216, 187–192.

Sager, W.W., 2002. Basalt core paleomagnetic data from Ocean Drilling Program Site 883 on Detroit Seamount, northern Emperor Seamount chain, and implications for the paleolatitude of the Hawaiian hotspot. Earth Planet Sci. Lett. 199, 347–358.

Shackleton, N.J., Opdyke, N.D., 1977. Oxygen isotope and palaeomagnetic evidence for early Northern Hemisphere glaciation. Nature 270, 216–219.

Sharp, W.D., Clague, D.A., 2006. 50-Ma initiation of Hawaiian-emperor bend records major change in Pacific Plate motion. Science 313, 1281–1284.

Skornyakova, N.S., Murdmaa, I.O., 1992. Local variations in distribution and composition of ferromanganese nodules in the Clarion-Clipperton Nodule Province. Mar. Geol. 103, 381–405.

Sun, W., Langmuir, C.H., Ribe, N.M., Zhang, L., Sun, S., Li, H., Li, C., Fan, W., Tackley, P. J., Sanan, P., 2021. Plume-ridge interaction induced migration of the Hawaiian-Emperor seamounts. Sci. Bull. 66, 1691–1697.

Sun, W., Zhang, L., Li, H., Liu, X., 2020. The synchronic Cenozoic subduction initiations in the west Pacific induced by the closure of the Neo-Tethys Ocean. Sci. Bull. 65, 2068–2071.

Tarduno, J., Bunge, H.-P., Sleep, N., Hansen, U., 2009. The bent Hawaiian-emperor hotspot track: inheriting the mantle wind. Science 324, 50–53.

Tarduno, J.A., Duncan, R.A., Scholl, D.W., Cottrell, R.D., Steinberger, B., Thordarson, T., Kerr, B.C., Neal, C.R., Frey, F.A., Torii, M., Carvallo, C., 2003. The Emperor Seamounts: southward motion of the Hawaiian hotspot plume in earth's mantle. Science 301, 1064–1069.

Uematsu, M., Duce, R.A., Prospero, J.M., Chen, L., Merrill, J.T., McDonald, R.L., 1983. Transport of mineral aerosol from Asia over the North Pacific ocean. J. Geophys. Res.: Oceans 88, 5343–5352.

van de Flierdt, T., Frank, M., Halliday, A.N., Hein, J.R., Hattendorf, B., Günther, D., Kubik, P.W., 2004a. Deep and bottom water export from the Southern Ocean to the Pacific over the past 38 million years. Paleoceanography 19, P1020.

van de Flierdt, T., Frank, M., Lee, D.-C., Halliday, A.N., Reynolds, B.C., Hein, J.R., 2004b. New constraints on the sources and behavior of neodymium and hafnium in seawater from Pacific Ocean ferromanganese crusts. Geochem. Cosmochim. Acta 68, 3827–3843.

Veizer, J., Ala, D., Azmy, K., Bruckschen, P., Buhl, D., Bruhn, F., Carden, G.A.F., Diener, A., Ebneth, S., Godderis, Y., Jasper, T., Korte, C., Pawellek, F., Podlaha, O.G., Strauss, H., 1999. ^{87}Sr/^{86}Sr, δ^{13}C and δ^{18}O evolution of Phanerozoic seawater. Chem. Geol. 161, 59–88.

Wegorzewski, A.V., Kuhn, T., 2014. The influence of suboxic diagenesis on the formation of manganese nodules in the Clarion Clipperton nodule belt of the Pacific Ocean. Mar. Geol. 357, 123–138.

Weiss, B.P., Lima, E.A., Fong, L.E., Baudenbacher, F.J., 2007. Paleomagnetic analysis using SQUID microscopy. J. Geophys. Res. Solid Earth 112, B09105.

Werner, R., Hoernle, K., Hauff, F., Portnyagin, M., Yogodzinski, G., Ziegler, A., 2016. RV SONNE Fahrtbericht/Cruise Report SO249, BERING - Origin and Evolution of the Bering Sea: an Integrated Geochronological, Volcanological, Petrological and Geochemical Approach. Helmholtz Centre for Ocean Research Kiel, Kiel, Germany, p. 454.

Wessel, P., Kroenke, L.W., 2009. Observations of geometry and ages constrain relative motion of Hawaii and Louisville plumes. Earth Planet Sci. Lett. 284, 467–472.

Westerhold, T., Marwan, N., Drury, A.J., Liebrand, D., Agnini, C., Anagnostou, E., Barnet, J.S.K., Bohaty, S.M., Vleeschouwer, D.D., Florindo, F., Frederichs, T., Hodell, D.A., Holbourn, A.E., Kroon, D., Lauretano, V., Littler, K., Lourens, L.J., Lyle, M., Pälike, H., Röhl, U., Tian, J., Wilkens, R.H., Wilson, P.A., Zachos, J.C., 2020. An astronomically dated record of Earth's climate and its predictability over the last 66 million years. Science 369, 1383–1387.

Wilson, J.T., 1963. A possible origin of the Hawaiian Islands. Can. J. Phys. 41, 863–870.

Xuan, C., Channell, J.E.T., 2008. Origin of orbital periods in the sedimentary relative paleointensity records. Phys. Earth Planet. In. 169, 140–151.

Yi, L., Medina-Elizalde, M., Kletetschka, G., Yao, H., Simon, Q., Paterson, G.A., Bourlès, D.L., Deng, X., Du, J., Qin, H., Chen, Y., Xie, Q., Xiao, J., Wang, Y., Andreucci, K., Keddadouche, K., Aumaître, G., Liu, Y., Wang, H., Shen, Z., Gu, X., Smith, T., Dang, H., Jian, Z., Song, T., He, H., Deng, C., Zhu, R., 2020. The potential of marine ferromanganese nodules from eastern pacific as recorders of earth's magnetic field changes during the past 4.7 Myr: a geochronological study by magnetic scanning and authigenic ^{10}Be/^{9}Be dating. J. Geophys. Res. Solid Earth 125, e2019JB018639.

Yi, L., Medina-Elizalde, M., Tan, L., Kemp, D.B., Li, Y., Kletetschka, G., Xie, Q., Yao, H., He, H., Deng, C., Ogg, J.G., 2023. Plio-Pleistocene deep-sea ventilation in the Eastern Pacific and potential linkages with Northern Hemisphere glaciation. Sci. Adv. 9, eadd1467.

Zachos, J., Pagani, M., Sloan, L., Thomas, E., Billups, K., 2001. Trends, rhythms, and aberrations in global climate 65 Ma to present. Science 292, 686–693.

Zeebe, R.E., 2007. Modeling CO_2 chemistry, δ^{13}C, and oxidation of organic carbon and methane in sediment porewater: implications for paleo-proxies in benthic foraminifera. Geochem. Cosmochim. Acta 71, 3238–3256.

Zhang, T., Fang, X., Song, C., Appel, E., Wang, Y., 2014. Cenozoic tectonic deformation and uplift of the South Tian Shan: implications from magnetostratigraphy and balanced cross-section restoration of the Kuqa depression. Tectonophysics 628, 172–187.

Zhang, T., Fang, X., Song, C., Appel, E., Wang, Y., 2017. Reply to the comment by. Erwin Appel, and Yadong Wang [Tectonophysics, 2014. In: Qiao, Q.Q., et al. (Eds.), Cenozoic Tectonic Deformation and Uplift of the South Tian Shan: Implications from Magnetostratigraphy and Balanced Cross-Section Restoration of the Kuqa Depression" by Tao Zhang, Xiaomin Fang, Chunhui Song, vol. 709, pp. 39–43. https://doi.org/10.1016/j.tecto.2014.04.044. Tectonophysics.

Zhong, Y., Chen, Z., González, F.J., Ortiz, J.E., Blanco, L., Marino, E., Liu, Q., 2021. Insights into the origin of ferromanganese-rich deposits associated with South China Sea contourite depositional systems. Mar. Petrol. Geol. 133, 105257.